https://doi.org/10.1038/s44306-024-00024-5

High-temperature Néel skyrmions in Fe_3GaTe_2 stabilized by Fe intercalation into the van der Waals gap

Rana Saha[1,2], **Holger L. Meyerheim**[1], **Börge Göbel**[3], **Ingrid Mertig**[3] & **Stuart S. P. Parkin**[1]

Two-dimensional (2D) van der Waals (vdW) magnets that exhibit ferromagnetism at ambient temperature show great promise for spintronic applications. However, until now, only a few pristine or doped 2D magnets have demonstrated the ability to host non-collinear spin textures, thereby limiting their potential applications. Here we directly observe Néel-type skyrmions in the metallic vdW magnetic compound Fe_3GaTe_2 (FGaT) up to temperatures well above room temperature (≈340 K) in the absence of any external magnetic field. We show that the presence of defects in the structure of FGaT make its structure acentric and therefore compatible with hosting skyrmions that would otherwise not be possible. Indeed, in this regard it is very similar to the closely related compound Fe_3GeTe_2 (FGT), whose structure with the same space group $P3m1$ is also realized by defects. Interestingly, however, FGaT accommodates a significantly higher concentration of Fe within the vdW gaps, likely accounting for its enhanced Curie temperature (T_C). In addition to the Néel skyrmions observed in the temperature range of 250–340 K, we also detect type-I and -II Bloch-type skyrmionic bubbles in the temperature range of 100–200 K due to an enhanced magnitude of dipole-dipole interactions relative to the Dzyaloshinskii-Moriya exchange interaction. Self-intercalation is thus a highly interesting property of vdW magnets that considerably modifies their fundamental properties.

Two-dimensional (2D) van der Waals (vdW) magnets constitute a versatile class of layered materials, providing the opportunity to finely tune long-range magnetic ordering through the modulation of magnetic interactions by altering the number of layers or the intercalation of magnetic atoms into the vdW gap[1–3]. This flexibility makes these materials promising candidates for spintronic applications at room temperature. A central theme in contemporary spintronics involves exploring spin structures that deviate from traditional parallel or anti-parallel alignments, manifesting non-collinear characteristics[4–6]. The pursuit of non-collinear magnetic structures, particularly topological spin textures like skyrmions[7] and anti-skyrmions[8], has garnered significant attention. These unique textures emerge from the interplay between Heisenberg exchange interactions and chiral Dzyaloshinskii-Moriya exchange interactions (DMI)[9,10]. The realization of the latter is generally linked to the absence of inversion symmetry, thus adding constraints to the selection of materials in which DMI emerges. Fe_3GeTe_2[11] (FGT) and $Cr_{1+\delta}Te_2$[12] have recently been shown to exhibit acentric crystal structures as well as Néel skyrmions, but the stability range of the skyrmions was limited to a temperature range near or below their Curie temperature (T_c) of ~220 K. The centrosymmetric 2D magnet, $Cr_2Ge_2Te_6$, has been shown to stabilize skyrmion bubbles at low temperatures (~60 K)[13].

Several efforts have been made in various FGT-type systems to enhance their Curie temperature. For example, attempts have been made to achieve this through ionic gating, albeit with limited success[14]. Other approaches that have been explored, include tuning the Fe concentration within the structure[15–17], Cobalt co-doping[18], high-pressure methods[19], and leveraging proximity effects with a topological insulator[20]. Using Co-doping, skyrmions could be stabilized above room temperature[18], which involves a structural phase transition of the Fe_5GeTe_2 structure from rhombohedral to primitive[21]. Recently it has been shown that in the iron-deficient $Fe_{3-x}GaTe_2$ compound Néel skyrmions can be stabilized above room temperature which was attributed to the symmetry lowering resulting from Fe vacancies giving rise to a strong DMI[22].

In this study we show that Fe_3GaTe_2 (FGaT) combines all the required prerequisites to stabilize Néel-type skyrmions well above room temperature

---

[1]Max Planck Institute of Microstructure Physics, Weinberg 2, Halle (Saale) 06120, Germany. [2]Department of Chemistry, Indian Institute of Science Education and Research, Yerpedu, Tirupati 517619, India. [3]Institute of Physics, Martin Luther University, Halle-Wittenberg, Halle (Saale) 06120, Germany.
e-mail: rana.saha@iisertirupati.ac.in; stuart.parkin@mpi-halle.mpg.de

(≈340 K) and in zero field, as directly observed by Lorentz transmission electron microscopy (LTEM). The enhanced temperature stability is related to a significant concentration of Fe atoms within the vdW gaps thereby enhancing the exchange interaction across the FGaT sheets. In close analogy to FGT, FGaT is characterized by a non-centrosymmetric structure (space group $P3m1$) as well as by a robust perpendicular magnetic anisotropy and an exceptionally high Curie temperature ($T_c \sim 370$ K). Moreover, within the same material, we reveal the stabilization of Bloch-type skyrmionic bubbles (type-I and -II) at low temperatures (100–200 K), attributed to long-range dipole-dipole interactions (DDIs).

Results and discussion

Single crystals of FGaT were synthesized by a self-flux method[23]. Their structural and magnetic properties were investigated by X-ray diffraction (XRD) and SQUID magnetometry, respectively. Previous reports have revealed that bulk FGaT crystallizes at room temperature in the inversion symmetric hexagonal space group (SGR) #194, $P6_3/mmc$[23]. Our XRD analysis using a Ga metal-jet X-ray source (wavelength, $\lambda = 1.341$ Å) which was carried out at both 9 and 300 K indicates a lower symmetry corresponding to $P3m1$ SGR (#156). Using a six-circle diffractometer equipped with a He-cryostat and a two-dimensional pixel detector[24], a total of 53 reflections were collected through transverse (θ) scans, reducing to 29 independent reflections through the point group symmetry ($3m$). Notably, reflections of type $HH2\bar{H}L$ with L being an odd number were observed, though they are very weak. An illustration in Fig. 1a the $(11\bar{2}3)$ reflection (see inset) and the symmetry-allowed $11\bar{2}6$ reflection are compared, demonstrating a several-order-of-magnitude difference in intensity. In SGR $P6_3/mmc$, reflections of type $HH2\bar{H}L$ with odd L are forbidden by symmetry. Thus, their observation suggests a lower crystal symmetry, related to one of the subgroups of $P6_3/mmc$ where such reflections are allowed. Subgroups satisfying this criterion are SGR $P\bar{3}2/m$ (SGR #164) and $P3m1$[11]. Specifically, the best fit of calculated structure factor magnitudes ($|F_{calc}(HKL)|$) to the observed ones ($|F_{obs}(HKL)|$), as quantified by the goodness-of-fit parameter (GOF) and unweighted residuum (R_U), indicates that the crystal structure of the FGaT plate belongs to the SGR $P3m1$ (#156). Values of GOF = 0.91 and $R_U = 0.082$[25] for the data collected at 9 K were obtained, which is discussed in the following.

The crystal structure of FGaT closely resembles that of FGT[11]. A schematic is shown in Fig. 1a. However, some variations are observed, namely the site occupancy factors (SOFs) for Wyckoff sites 1b, denoted as #5 and #6, which are equal to 52% and 60%, respectively, are smaller than those found in our previous study (92% and 85%). In combination with vertical atomic relaxations this SOF inequivalence contributes to lowering the symmetry from $P6_3/mmc$ to $P3m1$. The Fe deficiency at sites labeled by #5 and #6 is almost compensated by Fe intercalation into the two symmetry-independent vdW gaps labeled by vdW1 and vdW2 in Fig. 1a (~35–45% in FGaT), which is larger than found in FGT (7%) as detailed in the Supplementary Information, (SI). Thus, stoichiometry is almost preserved in both cases. The increased concentration of Fe residing within the vdW gaps is anticipated to increase the T_C in FGaT, fostering an enhanced exchange interaction between individual 2D sheets across these gaps. First-principles calculations on FGT, a compound structurally equivalent to FGaT, demonstrate that the introduction of Fe intercalation can significantly enhance the T_C[26]. The structure of FGaT is almost independent of temperature (9 K versus 300 K), the only difference being the vertical disorder of the split-site Ga atoms at 300 K. Figs. S1–S2 and Table S1 show the structure of the sample at 300 K and the comparison of the structural parameters at 9 and 300 K, respectively.

In Fig. 1b, we present the temperature-dependent magnetization curves, $M(T)$, obtained from a single crystal of FGaT (in the form of a flat plate) in the presence of a 0.1 T magnetic field applied both perpendicular (OP) and parallel (IP) to the crystal surface (0001). This measurement indicates a robust magnetic easy axis along [0001]. The Curie temperature (T_C), derived from the $M(T)$ curves, is approximately equal to 370 K. The inset of Fig. 1b displays the OP hysteresis loop, $M(\mu_0 H)$, at three temperatures, emphasizing the soft ferromagnetic nature (the coercive field, $H_C \sim 10$ Oe at 300 K) within the measured temperature range.

The non-centrosymmetric and polar structure of FGaT, identified by XRD, is characterized by the C_{3v} point group symmetry, which allows for the hosting of certain non-collinear spin textures[27]. To investigate these magnetic textures, LTEM[28] was performed on a wedge-shaped lamella prepared from a single crystal of FGaT through ion beam milling with a Gallium Focused Ion Beam (FIB) system. In Fig. S3, we display the scanning electron microscopy (SEM) image of a wedge-shaped lamella. The LTEM experiment employed a double-tilt liquid nitrogen sample holder capable of a temperature variation within the range of 100–380 K, conducted inside an electron microscope operating at an accelerating voltage of 200 keV.

Initially, the [0001] zone-axis of the lamella which is the polar axis of the crystal's C_{3v} point group was aligned parallel to the incident electron beam. The lamella was heated above its T_C and then cooled to room

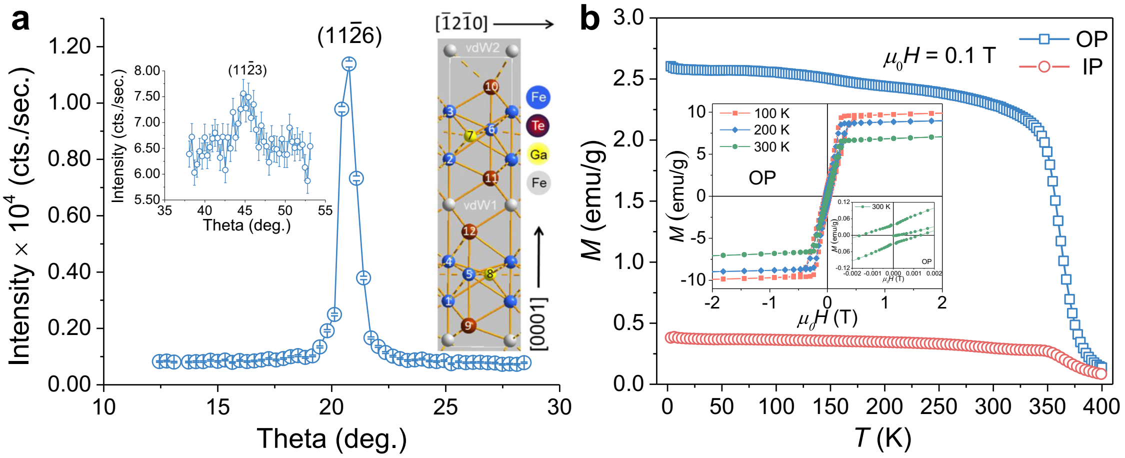

Fig. 1 | Structure and magnetic properties of Fe_3GaTe_2 single crystal. **a** Comparison of theta scans across the $(11\bar{2}6)$ reflection of the Fe_3GaTe_2 crystal. The inset shows the scan across the $(11\bar{2}3)$ reflection which in SGR $P6_3/mmc$ is forbidden. The latter type of reflections is typically several orders of magnitude weaker than the allowed ones. The schematic of the crystal structure viewed along the $[11\bar{2}0]$ direction is shown in right, where atoms are numbered according to Table S1 in the Supplementary Information and vdW1, vdW2 indicate the two symmetry-independent van der Waals gaps within the unit cell. Colored spheres represent Te, Fe, and Ga atoms as labeled. **b** Temperature (T) dependence of the magnetization (M) for the Fe_3GaTe_2 crystal is shown for the magnetic field ($\mu_0 H$) applied along the out-of-plane (OP) and the in-plane (IP) direction with respect to the (0001) surface of the single crystalline platelet. The inset displays the isothermal magnetization versus magnetic field applied along the OP direction at 100, 200, and 300 K. The smaller inset inside M vs. $\mu_0 H$ plot shows the magnified data at 300 K.

temperature in the absence of any external field. Subsequently, LTEM images were collected under varying magnetic fields. No magnetic contrast was observed when the LTEM images were recorded with the electron beam parallel to [0001]. However, tilting away from the [0001] axis revealed cycloidal stripe domains at zero magnetic field across the wedge (see Fig. S4).

Field-cooling (FC) from 380 K to room temperature under a 51 mT magnetic field applied along the [0001] axis resulted in LTEM images showing no magnetic contrast when imaged along [0001]. Tilting away from the [0001] axis, up to a maximum angle of 29°, led to the emergence of a circular magnetic contrast with half-dark and half-bright regions at their opposite edges which is characteristic for Néel-type skyrmions[12]. Additional LTEM images recorded by tilting the sample about both the x-axis and y-axis are provided in the SI (see Fig. S5). In contrast, when subject to field-cooling from 380 K to room temperature under an applied magnetic field of 12 and 24 mT, the formation of a stripe phase or a combination of stripes and magnetic skyrmions is observed. The field-cooling process is crucial for stabilizing the metastable skyrmion lattice, because in the absence of the magnetic field, the FGaT has a tendency to form cycloidal stripe domains. These domains undergo a direct transformation into the field-polarized (FP) state when a magnetic field is applied, i.e., without the stabilization of the skyrmion lattice.

Figure 2 displays the LTEM images of Néel-type skyrmions for three distinct thickness regions in the same wedge (A1: 146 nm; A2: 207 nm; A3: 232 nm). No magnetic contrast is observed under 0° and 3.4° tilting conditions, as illustrated in Fig. 2a, b. To further confirm the Néel-type nature of these spin textures, additional LTEM experiments were carried out, revealing an enhanced magnetic contrast with increasing tilting which indicates an enhanced asymmetric deflection of the incident electrons induced by the increased in-plane component of the magnetization related to the Néel-type skyrmions (Fig. 2c–f). Additionally, the examination of field variation at a fixed angle shows the gradual transformations of Néel-type skyrmions into the FP state, as illustrated in Fig. S6. The LTEM images in Fig. 2 clearly show that the size of the magnetic textures increases with the thickness of the lamella (also see Fig. 4b). This observation emphasizes the substantial impact of DDI on the behavior of the magnetic textures[29].

We now present the results from LTEM imaging at 100 K. First, the wedge lamella was subjected to field-cooling from 380 K to 100 K in the presence of a 51 mT magnetic field applied along the [0001] direction. Upon temperature stabilization, LTEM images were acquired along the [0001] direction, revealing magnetic contrast typical of type-I bubbles[30], as shown in Fig. 3a (also see Fig. S7a in SI). The textures are topologically equivalent to the skyrmions observed before but are of Bloch-type instead of Néel-type for which the magnetic contrast only appeared under tilting away from [0001] (see Fig. S7b). Following the stabilization of type-I bubble lattice with field-cooling, we subsequently reduced the magnetic field to zero and observed that the lattice remained stable at zero field in all three thickness regions. To enhance the magnetic contrast, images were recorded under a 5° tilting, as depicted in Fig. 3b. We then varied the magnetic field at intervals of 25 mT until the entire sample became field-polarized.

In Fig. 3c–f, LTEM images under a 5° tilting are presented at selected magnetic fields for three distinct thickness regions. In Fig. 3c, it is evident that type-I bubbles with two different helicities exist across all thickness regions, as marked by the red squares. Intriguingly, as the magnetic field increases to 201 mT, a few type-II bubbles appear, coexisting with type-I bubbles, as indicated by the yellow square in Fig. 3d. With a further increment of the magnetic field to 252 mT, the density of magnetic bubbles decreases. Eventually, at a magnetic field of 300 mT, all magnetic bubbles vanish and the FP state emerges. The coexistence of magnetic objects with two different helicities signifies the dominance of the DDI over the DMI[31], although the structure is non-centrosymmetric at all temperatures, which is evidenced by XRD and temperature-dependent SAED pattern as shown in Fig. S8.

Following these observations, LTEM images were recorded over a temperature range between 100 and 300 K, as well as above room temperature, following a similar FC process, as shown in Fig. S9 in the SI. The observations are summarized in the magnetic field vs. temperature phase diagram presented in Fig. 4a. Here we show the results for the thinner part of the wedge (A1: 146 nm). While the phase diagram qualitatively resembles those of the thicker parts of the sample (A2: 207 nm and A3: 232 nm) [see Fig. S10], the formation of the FP state requires a higher magnetic field which is attributed to an enhanced dipolar interaction. The phase diagram indicates that magnetic bubbles are stable in the temperature range between 100 and 200 K, while above 250 K, Néel-type skyrmions emerge which are stable up to ~340 K even in the absence of an external field. Although the Curie temperature is ~370 K, the LTEM contrast becomes weaker after 340 K as a result of decreased magnetization as seen in Fig. 1b. Figure 4b,

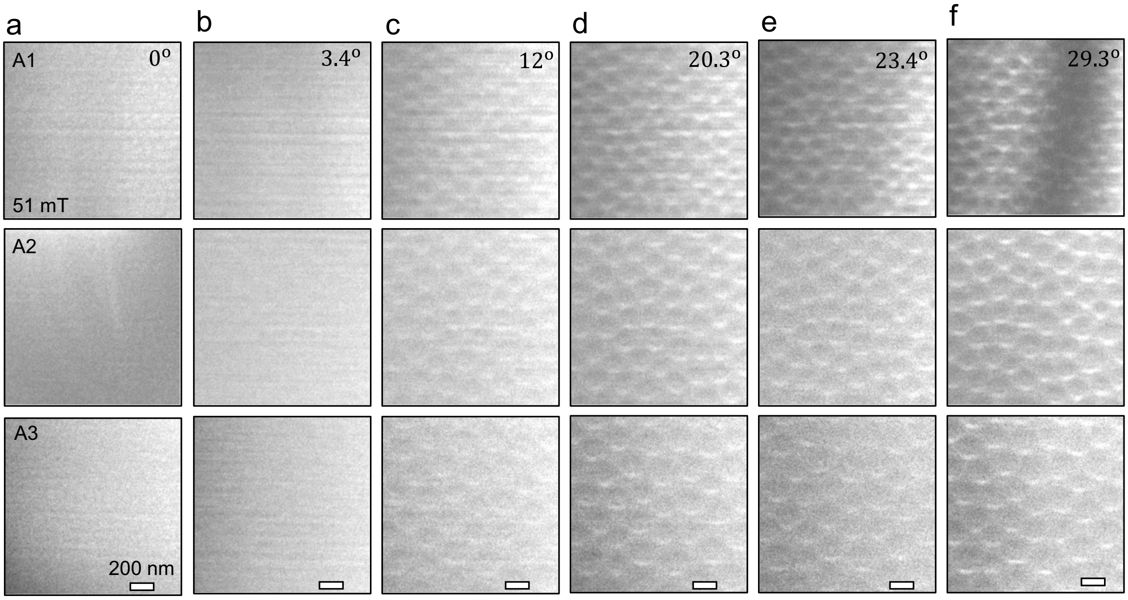

Fig. 2 | Lorentz Transmission Electron Microscopy (LTEM) images of the wedge-shaped lamella of Fe_3GaTe_2 at 300 K under various tilting angles away from the [0001] direction. a–f Sequence of tilting-angle-dependent LTEM images recorded at 300 K in the presence of a 51 mT magnetic field after field-cooling. Three distinct lamella thicknesses along the wedge-shaped lamella are studied: A1: 146 nm, A2: 207 nm, and A3: 232 nm. Bending contours are observed in region A1 (e.g., in **f**). Image dimension in (**a**–**f**) is 1.5 × 1.5 µm^2 (see scale bar of 200 nm) in each LTEM image. All images are taken at a defocus of −1.0 mm.

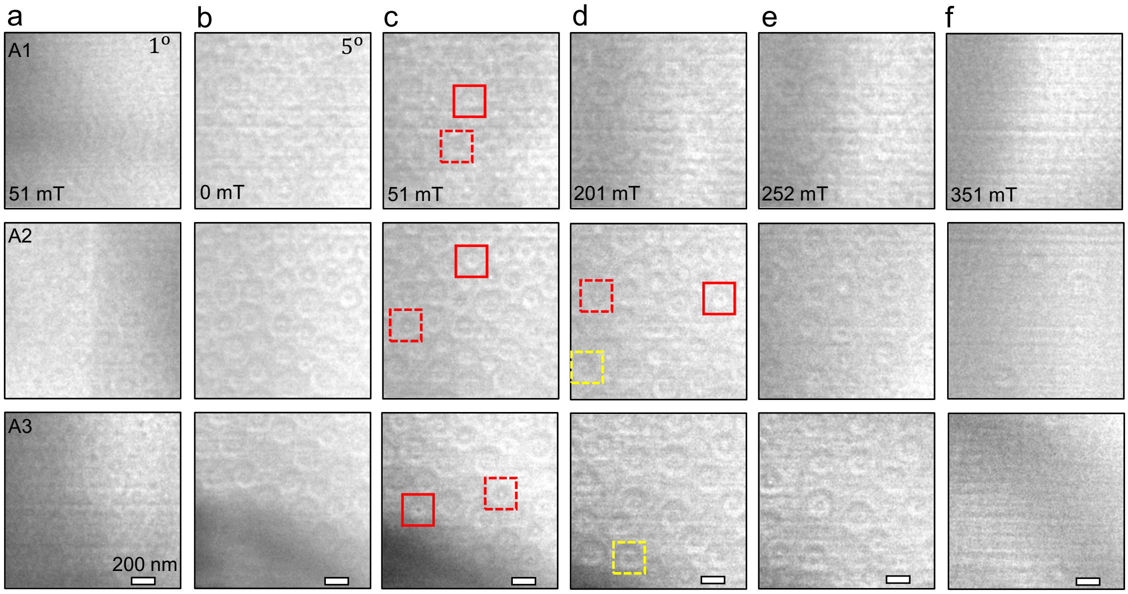

Fig. 3 | LTEM images of the wedge-shaped lamella of Fe_3GaTe_2 at 100 K under varying magnetic fields. **a**–**f** Sequential magnetic-field-dependent LTEM images recorded at 100 K after field-cooling by applying a 51 mT magnetic field for three distinct thickness regions (A1: 146 nm, A2: 207 nm, and A3: 232 nm) of the wedge-shaped lamella. LTEM images in (**b**–**f**) were acquired under a 5° tilting angle, while the image in (**a**) was recorded close to the [0001] direction. Solid and dashed red boxes highlight type-I bubbles with opposite helicity, and the yellow dashed box denotes type-II magnetic bubbles. Image's size in (**a**–**f**) is 1.5 × 1.5 μm^2, the scale is 200 nm in each LTEM image. All images are taken at a defocus of −1.0 mm.

shows the diameter of the magnetic objects at zero magnetic field versus temperature, which is nearly constant. Only the long-range DDI induces an increase of the bubble (and skyrmion) size with increasing sample thickness.

To elucidate the stability of skyrmions with different helicities we have carried out micromagnetic simulations (Fig. 4c, d) using the code mumax3[32,33] (see Methods for details). The experimental observations are qualitatively reproduced, i.e., Bloch-type skyrmionic bubbles are stable at lower temperatures, mainly stabilized by DDI, while, at higher temperatures Néel skyrmions emerge, and stabilized by the DMI.

The transition from the bubble state to the skyrmionic state with increasing temperature is related to the reduced magnitude of the DDI relative to the DMI resulting from a decreasing net magnetization (M_S). The behavior can be qualitatively modeled by starting with a large M_s that stabilizes Bloch-type skyrmionic bubbles characterized by opposite helicities $\pm \sim \frac{\pi}{2}$ as shown in panels #2 and #13 in Fig. 4c, d, respectively. These skyrmionic bubbles correspond to the circularly shaped LTEM contrast in Fig. 3 which are well reproduced by LTEM image simulations shown on the left of Fig. 4c, d in panels #1 and #12 (see Methods for details). Since this spin texture is dominated by the larger DDI relative to the DMI, Bloch skyrmions with opposite helicities can simultaneously exist for the same material parameters. Reduction of M_s (effectively corresponding to the experimental temperature increase) enhances the relevance of the DMI and the Bloch-type textures turn into equivalent Néel skyrmions with the helicity of ~0 (panels #10 and #21 in Fig. 4c, d, respectively). The helicity determines the in-plane orientation of the magnetic moments. It is defined as the difference of the polar angles of the magnetic moments of a skyrmion and the corresponding position vectors[34]. In accordance with experiment no LTEM contrast is observed in the simulation under normal incidence condition, while only in the case of sample tilting two opposite circular contrasts are revealed (see panels #11 and #22 in Fig. 4c, d), which is the characteristic signature of Néel skyrmions as shown in Fig. 2.

Micromagnetic simulations (Fig. 4c, d) agree qualitatively with the LTEM measurements presented in Figs. 2 and 3. They reveal the physical mechanism governing the stability of distinct nano-magnetic objects in the same FGaT crystal: The coexistence of a finite magnitude of the DMI to the DDI favor Néel- and Bloch-type skyrmions, respectively. The presence of competing interactions in which the relative magnitude of the DMI to the DDI governs the emergence of different nano-magnetic objects has been observed previously in D_{2d} symmetric Heusler compounds that host both skyrmions and anti-skyrmions[31]. These materials are characterized by an anisotropic DMI, so that Bloch skyrmions and anti-skyrmions can coexist. However, these textures cannot be continuously transformed from one to another upon changing the temperature because they are topologically distinct (the topological winding number, $N_{Sk} = +1$ vs. -1) and the topological charge can only have integer values. Therefore, intermediate configurations[35] are not stable. The texture is either a Bloch skyrmion or an anti-skyrmion.

In the case of FGaT, the isotropic DMI stabilizes Néel skyrmions that are topologically equivalent to the DDI-stabilized Bloch skyrmionic bubbles (type-I). Since both objects have the same N_{Sk}, one can identify stable intermediate states[35] between the two as in panels #6 and #17 of Fig. 4c, d. For these states the helicity is neither 0 nor $\pm \frac{\pi}{2}$[7,34]. However, due to the lack of a topologically-induced energy barrier between the Bloch and Néel configurations, the two cannot coexist. This distinct consequence of the same mechanism in D_{2d} inverse Heusler compounds and FGaT highlights the significance of topology and 'topological protection' for skyrmionic spin textures.

In the experimental LTEM images in Fig. 3, tilting of the sample increases the LTEM contrast (comparing panels a and b). This indicates that the helicity of these textures is likely not perfectly Bloch-like but that Néel components are present as well. As a consequence, the magnetic configuration is rather an intermediate state between Bloch and Néel skyrmion stabilized by the interplay of DMI and DDI and can be controlled by changing the temperature.

Conclusion

In summary, our comprehensive investigations, combining experimental techniques and micromagnetic simulations, uncovers the presence of Néel skyrmions and skyrmion bubbles in the 2D vdW compound FGaT within the temperature ranges of 250–340 K and 100–200 K, respectively. XRD analysis reveals a significant concentration of Fe atoms (≈35%) within the two symmetry-independent vdW gaps of the unit cell, which likely accounts for the high T_C of 370 K owing to the enhanced exchange interaction between the FGaT sheets mediated by the self-intercalated Fe atoms. For

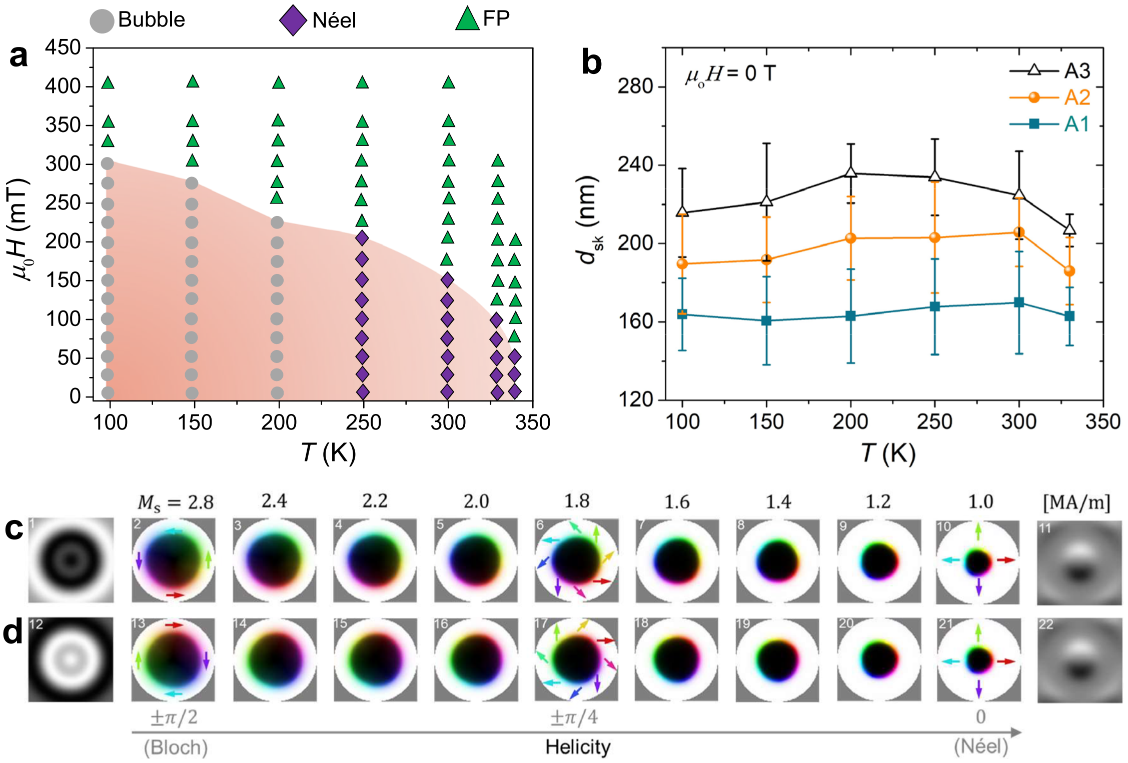

Fig. 4 | Magnetic phase diagram, thickness-dependent size of magnetic textures at different temperatures, and micromagnetic simulation of the transformation from Bloch-type bubbles to Néel skyrmions. a Magnetic phase diagram showing the relationship between temperature (T) and magnetic field (μ_0H) for the lamella thickness of 146 nm, obtained after field-cooling with a 51 mT magnetic field. The red area represents the region occupied by either bubbles or Néel-type skyrmions, denoted by symbols: ● for magnetic bubbles, ◆ for Néel-type skyrmions, ▲ and for the field-polarized (FP) phase. Symbols indicate the magnetic field and temperature where LTEM images were collected. Skyrmion diameter (d_{sk}) versus temperature (T) in regions A1, A2, and A3. Error bars in (**b**) represent the standard deviation of d_{sk}. **c**, **d** *Micromagnetic simulations*. Two Bloch skyrmions with opposite helicities of $+\pi/2$ (top row: panels 1–11) and $-\pi/2$ (bottom row: panels 12–22) are stabilized under different saturation magnetization values M_s, as indicated in top of panels 2–11. In the top row, the counter-clockwise Bloch skyrmion gradually transforms into a Néel skyrmion by decreasing M_s. The color indicates the orientation of the magnetic moments, with black and white representing out-of-plane orientations and colors indicating in-plane orientations, as indicated by arrows. Panels (1) and (11) in the top row show the simulated LTEM contrasts corresponding to type-I Bloch-bubble (2) and Néel-type skyrmion (10), respectively. The bottom row (12–22) follows the same process but starts with a clockwise Bloch skyrmion.

FGaT its properties cannot be understood without appreciation of the significant and natural structural distortions that we have found. While the sample preparation may play a role in these distortions, we note that typically stoichiometric mixtures are used to prepare single crystals and, nevertheless, one finds significant amounts of Fe within the vdW gaps, as here. These distortions lower the symmetry of FGaT to the non-centrosymmetric and polar space group $P3m1$. This makes possible the two distinct chiral non-collinear spin textures that we find. It is remarkable that two spin textures exist in a single acentric 2D compound, particularly under zero magnetic field conditions and at specific temperatures.

Methods

Structural and magnetic characterization

The XRD experiments were carried out with a Gallium Jet X-ray source operating at an acceleration voltage of 70 kV and a power of 200 W, emitting Ga-Kα radiation (λ = 1.341 Å) monochromatized with Montel optics. Diffracted peak intensities were captured using a six-circle diffractometer and a two-dimensional Pilatus 100k pixel detector. Temperature-dependent experiments were conducted in a helium-cooled Cryovac Konti Micro cryostat. Integrated intensities of the diffraction peaks, crucial for structure analysis, were acquired through transverse (theta-) scans. These scans underwent subsequent correction factors (Lorentz-, polarization, effective area, absorption) to determine the structure factor magnitudes. The temperature and field (μ_0H) dependent magnetization (M) measurements of the single crystal of Fe_3GaTe_2 were performed using a SQUID-VSM [MPMS3, Quantum Design].

Transmission electron microscopy

For transmission electron microscopy (TEM) investigations, multiple lamellae from the same single crystal of Fe_3GaTe_2 were prepared via Focused Ion Beam (FIB) Ga^+ ion milling [FEI Nova Nanolab 600 SEM/FIB operating at 30 keV ion-beam energy] using standard lift-out procedures. Final polishing of the lamellae occurred with lower Ga^+ ion-beam energies (5 keV) to minimize the thickness of any amorphous surface layers. The lamella thickness, denoted as 'A', was measured from cross-sectional SEM images. Magnetic textures were imaged by TEM [JEOL JEM-F200] in the Lorentz mode operating at an accelerating voltage of 200 keV, using a GATAN double-tilt sample holder capable of varying the temperature between 100 and 380 K. A vertical magnetic field applied to the lamella within the TEM column was achieved by passing currents through the coils of the objective lens, and a Lorentz mini-lens was employed for imaging.

Calculation of Lorentz TEM image contrast

We conducted calculations of Lorentz TEM images using the approach described in ref. 31. The contrast at position (x, y) arises from the density of transmitted electrons and is expressed by the integral:

$$\int \exp \frac{-[(x - d \cdot m_y(x', y') - x')^2 + (y + d \cdot m_x(x', y') - y')^2]}{a^2} \mathrm{d}x' \, \mathrm{d}y'.$$

We approximated the electron beams as Gaussian functions with a smearing factor a = 10 nm. The Lorentz force induces a transverse deflection of the incoming electron beams due to the averaged magnetization $\boldsymbol{m}(\boldsymbol{r})$

along the layers. The maximum deflection is regulated by $d = 1$ nm. Bloch skyrmions (panels #1 and #12 in Fig. 4c, d) have been simulated from the perpendicular direction. Néel skyrmions (panels #11 and #22 in Fig. 4c, d) have been simulated at a tilting angle of 10°.

Micromagnetic simulations

For the micromagnetic simulations we propagated two analytically constructed Bloch skyrmions towards the local energetically minimum. This gave rise to the two Bloch skyrmions presented on the left of Fig. 4c, d. We used mumax3[32,33] to propagate the Landau-Lifshitz-Gilbert equation[36,37]

$$\dot{\mathbf{m}} = -\gamma_e \mathbf{m} \times \mathbf{B}_{\mathrm{eff}} + \alpha \mathbf{m} \times \dot{\mathbf{m}}.$$

Here, $\mathbf{B}_{\mathrm{eff}} = \frac{-\delta F}{M_S \delta \mathbf{m}}$ is the effective magnetic field, calculated from the free energy F comprising the exchange interaction ($A = 15$ pJ/m), the uniaxial anisotropy ($K = 1.2$ MJ/m^3), a Zeeman interaction with a magnetic field ($B = 100$ mT), the Néel-type DMI ($D = 3.5$ mJ/m^2), and the dipole-dipole interaction. We have scaled the saturation magnetization from $M_s = 2.8$ MA/m, giving rise to almost perfect Bloch-type skyrmionic bubbles, down to $M_s = 1.0$ MA/m. Upon reducing M_s both Bloch skyrmions turned into the same Néel skyrmion as shown in panels #11 and #22 of Fig. 4c, d. The Gilbert damping is $\alpha = 0.3$ and γ_e is the gyromagnetic ratio. We simulate a nano-disk with diameter 100 nm and a thickness of 30 nm. The cell size in the simulations is 1 nm × 1 nm × 1 nm.

Received: 27 February 2024; Accepted: 11 April 2024;

References

1. Wang, Q. H. et al. The magnetic genome of two-dimensional van der Waals materials. *ACS nano* **16**, 6960 (2022).
2. Parkin, S. S. P. & Friend, R. 3d transition-metal intercalates of the niobium and tantalum dichalcogenides. I. Magnetic properties. *Philos. Mag. B* **41**, 65 (1980).
3. Parkin, S. S. P., Marseglia, E. & Brown, P. Magnetic structure of $Co_{1/3}NbS_2$ and $Co_{1/3}TaS_2$. *J. Phys. C: Solid State Phys.* **16**, 2765 (1983).
4. Yang, S.-H., Naaman, R., Paltiel, Y. & Parkin, S. S. P. Chiral spintronics. *Nat. Rev. Phys.* **3**, 328 (2021).
5. Parkin, S. S. P., Hayashi, M. & Thomas, L. Magnetic domain-wall racetrack memory. *Science* **320**, 190 (2008).
6. Fert, A., Cros, V. & Sampaio, J. Skyrmions on the track. *Nat. Nanotechnol.* **8**, 152 (2013).
7. Nagaosa, N. & Tokura, Y. Topological properties and dynamics of magnetic skyrmions. *Nat. Nanotechnol.* **8**, 899 (2013).
8. Nayak, A. K. et al. Magnetic antiskyrmions above room temperature in tetragonal Heusler materials. *Nature* **548**, 561 (2017).
9. Dzyaloshinsky, I. A thermodynamic theory of "weak" ferromagnetism of antiferromagnetics. *J. Phys. Chem. Solids* **4**, 241 (1958).
10. Moriya, T. Anisotropic superexchange interaction and weak ferromagnetism. *Phys. Rev.* **120**, 91 (1960).
11. Chakraborty, A. et al. Magnetic Skyrmions in a Thickness Tunable 2D Ferromagnet from a Defect Driven Dzyaloshinskii-Moriya Interaction. *Adv. Mater.* **34**, 2108637 (2022).
12. Saha, R. et al. Observation of Néel-type skyrmions in acentric self-intercalated $Cr_{1+\delta}Te_2$. *Nat. Commun.* **13**, 1 (2022).
13. Han, M.-G. et al. Topological magnetic-spin textures in two-dimensional van der Waals $Cr_2Ge_2Te_6$. *Nano Lett.* **19**, 7859 (2019).
14. Deng, Y. et al. Gate-tunable room-temperature ferromagnetism in two-dimensional Fe_3GeTe_2. *Nature* **563**, 94 (2018).
15. May, A. F. et al. Ferromagnetism near room temperature in the cleavable van der Waals crystal Fe_5GeTe_2. *ACS nano* **13**, 4436 (2019).
16. Seo, J. et al. Nearly room temperature ferromagnetism in a magnetic metal-rich van der Waals metal. *Sci. Adv.* **6**, eaay8912 (2020).
17. Wang, H. et al. Interfacial engineering of ferromagnetism in wafer-scale van der Waals Fe_4GeTe_2 far above room temperature. *Nat. Commun.* **14**, 2483 (2023).
18. Zhang, H. et al. Room-temperature skyrmion lattice in a layered magnet $(Fe_{0.5}Co_{0.5})_5GeTe_2$. *Sci. Adv.* **8**, eabm7103 (2022).
19. Li, Z. et al. Magnetic anisotropy control with curie temperature above 400 K in a van der waals ferromagnet for spintronic device. *Adv. Mater.* **34**, 2201209 (2022).
20. Wang, H. et al. Above room-temperature ferromagnetism in wafer-scale two-dimensional van der Waals Fe_3GeTe_2 tailored by a topological insulator. *ACS nano* **14**, 10045 (2020).
21. May, A. F., Du, M.-H., Cooper, V. R. & McGuire, M. A. Tuning magnetic order in the van der Waals metal Fe_5GeTe_2 by cobalt substitution. *Phys. Rev. Mater.* **4**, 074008 (2020).
22. Li, Z. et al. Room-temperature sub-100 nm Néel-type skyrmions in non-stoichiometric van der Waals ferromagnet $Fe_{3-x}GaTe_2$ with ultrafast laser writability. *Nat. Commun.* **15**, 1017 (2024).
23. Zhang, G. et al. Above-room-temperature strong intrinsic ferromagnetism in 2D van der Waals Fe_3GaTe_2 with large perpendicular magnetic anisotropy. *Nat. Commun.* **13**, 5067 (2022).
24. Moritz, W. & Van Hove, M. A. *Surface Structure Determination by LEED and X-rays*. (Cambridge University Press, 2022).
25. Abrahams, S. Indicators of accuracy in structure factor measurement. *Acta Crystallogr. Sec. A Crystal Phys. Diffr. Theor. Gen. Crystallogr.* **25**, 165 (1969).
26. Wu, Y. et al. Fe-Intercalation Dominated Ferromagnetism of van der Waals Fe_3GeTe_2. *Adv. Mater*. **35,** 2302568 (2023).
27. Tokura, Y. & Kanazawa, N. Magnetic skyrmion materials. *Chem. Rev.* **121**, 2857 (2020).
28. Pollard, S. D. et al. Observation of stable Néel skyrmions in cobalt/palladium multilayers with Lorentz transmission electron microscopy. *Nat. Commun.* **8**, 14761 (2017).
29. Ma, T. et al. Tunable Magnetic Antiskyrmion size and helical period from nanometers to micrometers in a D_{2d} Heusler compound. *Adv. Mater.* **32**, 2002043 (2020).
30. Loudon, J. C. et al. Do images of Biskyrmions show Type-II Bubbles? *Adv. Mater.* **31**, 1806598 (2019).
31. Jena, J. et al. Elliptical Bloch skyrmion chiral twins in an antiskyrmion system. *Nat. Commun.* **11**, 1115 (2020).
32. Vansteenkiste, A. et al. The design and verification of MuMax3. *AIP Adv*. **4**, 107133 (2014).
33. Vansteenkiste, A. & Van de Wiele, B. MuMax: a new high-performance micromagnetic simulation tool. *J. Magn. Magn. Mater.* **323**, 2585 (2011).
34. Göbel, B., Mertig, I. & Tretiakov, O. A. Beyond skyrmions: review and perspectives of alternative magnetic quasiparticles. *Phys. Rep.* **895**, 1 (2021).
35. Kim, K.-W., Moon, K.-W., Kerber, N., Nothhelfer, J. & Everschor-Sitte, K. Asymmetric skyrmion Hall effect in systems with a hybrid Dzyaloshinskii-Moriya interaction. *Phys. Rev. B* **97**, 224427 (2018).
36. Gilbert, T. L. A phenomenological theory of damping in ferromagnetic materials. *IEEE T. Magn.* **40**, 3443 (2004).
37. Landau, L. & Lifshitz, E. *On the theory of the dispersion of magnetic permeability in ferromagnetic bodies*. (Elsevier, 1992).

Acknowledgements

We acknowledge the funding provided by the Deutsche Forschungsgemeinschaft (DFG, German Research Foundation) – SPP 2137 (project number - 403505322) and SPP 2244 (project number - 443406107). We would like to thank Norbert Schammelt for his assistance in preparing TEM lamellae and Katayoon Mohseni for her help to carry out the structural analysis. We thank Hao Wu and Haixin Chang for providing the single crystals used in this study.

Author contributions

R.S. performed the Lorentz TEM experiments, analyzed the images, and conducted the magnetic characterization. H.L.M. conducted X-ray diffraction measurements. B.G. performed micromagnetic and LTEM image simulations under the supervision of I.M. The manuscript was written by R.S., H.L.M., B.G., and S.S.P.P. The study was conceived by R.S. and S.S.P.P. All authors participated in data discussions and provided comments on the manuscript.

Funding

Open Access funding enabled and organized by Projekt DEAL.

Competing interests

The authors declare no competing interests.

Additional information

Supplementary information The online version contains supplementary material available at https://doi.org/10.1038/s44306-024-00024-5.

Correspondence and requests for materials should be addressed to Rana Saha or Stuart S. P. Parkin.